PERGAMON

International Journal of Heat and Mass Transfer 42 (1999) 2143–2159

International Journal of HEAT and MASS TRANSFER

Salt-finger convection generated by thermal and solutal capillary motion in a stratified fluid

C.L. Chan*, C.F. Chen

Department of Aerospace and Mechanical Engineering, The University of Arizona, Tucson, AZ 85721, U.S.A.

Received 26 March 1998; in final form 22 September 1998

Abstract

Experiments and numerical simulations were performed to study the onset of finger convection in a stratified fluid layer caused by thermal and solutal capillary motion. Experiments were performed in a stratified ethanol–water solution contained in a shallow tank. Capillary motion was generated by a 2°C temperature difference maintained between the sidewalls. It caused the onset of finger convection by bringing relatively warm and solute-rich fluid on top of relatively cooler solute-poor fluid. A two-dimensional numerical simulation at early times prior to the onset of finger convection was carried out. The results clearly show the interactive effects of thermal and solutal capillary motion.

Nomenclature

D mass diffusivity
g gravitational acceleration
H thickness of the fluid layer
Le Lewis number
$M_{S,T}$ solutal and thermal Marangoni number
Pr Prandtl number
$Ra_{S,T}$ solutal and thermal Rayleigh number
S solute concentration
t time
T temperature
u, v x- and y-component of the velocity
x, y Cartesian coordinate system with y in the negative g-direction.

Greek symbols

$\beta_{S,T}$ solutal and thermal coefficients of volumetric expansion
γ surface tension
ΔS concentration difference
ΔT temperature difference
κ thermal diffusivity
ν kinematic viscosity
$\sigma_{S,T}$ surface tension gradients with respect to S and T
ψ stream function
ω vorticity.

1. Introduction

Recent experiments conducted by Chen and Chen [1] showed that salt-finger convection can be generated by capillary motion along the free surface in a tank of ethanol–water solution stably stratified by the water concentration. The motion is driven by surface tension gradients due to both thermal and solutal effects caused by a small temperature difference, ~ 1°C, across the tank. Buoyant cellular convection in the form of a vertical array of nearly horizontal cells as observed by Thorpe et al. [2] and Chen et al. [3] are absent because the critical ΔT for onset of such convection is much higher than 1°C for the initial density gradient in the fluid [2, 3]. At this low ΔT, the buoyant convection is in the stable region and the motion is almost imperceptible due to the stabilizing effect of the solute gradient. When the surface-tension-driven convection is well established, the flow on the free surface is from the hot to the cold wall, with a slow return flow in the opposite direction underneath. The surface streams are relatively solute rich while the return flow is relatively solute poor. This situation is favorable for the onset of salt fingers and, furthermore, the fingers occur

* Corresponding author. Tel.: 001 520 621 2235; fax: 001 520 621 8191; e-mail: chan@ame.arizona.edu

0017–9310/99/$ - see front matter
PII: S0017–9310(98)00329–9

in the presence of shear. Linden [4] and Thangam and Chen [5] showed, under such circumstances, that finger convection appears as longitudinal rolls aligned in the direction of shear. Linden [4] generated salt fingers in the presence of shear by a counterflow of sugar solution over a salt solution of greater density. The longitudinal rolls appeared in shadowgraphs as alternate dark and bright bands aligned in the direction of shear. Thangam and Chen [5] generated such flows by discharging a heated saline jet on the surface of a long tank of fluid stably stratified by salt at rest. Visualization was obtained by Schlieren photographs, which exhibited the longitudinal structures. Chen and Chen [1] used particle trace photography for visualization in their experiments. They observed finger convection by the presence of longitudinal rolls in the direction of shear. They further observed that the onset of finger convection occurred near the cold wall due to solutal capillary effects.

In order to better understand the influence of thermal and solutal capillary effects on the onset of finger convection, we have carried out more detailed experiments in a shallow tank. With the smaller physical dimensions, the problem became amenable to numerical simulations. In particular, we carried out a two-dimensional numerical simulation for the early times, up to the onset of finger convection, approximately 2 min after the start of the experiment. Many results of numerical simulations of problems related to the present one have been presented in the literature. The more recent ones are briefly reviewed here.

Direct numerical simulations of two-dimensional salt fingers were first carried out by Piacsek and Toomre [6] for a system with a hot and salty fluid layer on top of a cold and fresh fluid layer. Perturbation to the temperature and salinity fields was introduced to the quiescent fluid layers. Evolution of the fingers and associated fluxes were computed and the nonlinear growth rate was determined. It was found that the salt fingers developed bulbous tips near their ends, and these could detach and proceed ahead of the fingers, similar to that which had been observed in earlier experiments. Their computations were carried out in a comparatively short time period, approximately 7 Brunt-Väisälä periods, due to the limitation of the domain boundary, which contained approximately 16 fingers.

Shen [7] extended the calculations to a much larger computational domain consisting of approximately 50 fingers and found that the bulbous structures detached from the fingers, evolved into mushroom-shaped plumes, and eventually turned into turbulence at the end of approximately 30 Brunt-Väisälä periods. This study clearly showed that the fastest growing finger mode dominated the evolution of finger convection. However, the horizontal wavenumber spectrum suggested that the energy transferred from short-scale fingers to long-scale ones. Shen and Veronis [8] used the same numerical procedure to study the evolution of fingers in a Hele Shaw cell.

For two-dimensional thermocapillary-buoyancy driven convection problems, we confine our attention to rectangular geometries. Hadid and Roux [9] simulated the thermocapillary convection in a horizontal layer with a low Prandtl number fluid subject to a horizontal temperature gradient. They found a complex flow structure with multiple cells as the Reynolds number was increased. Using the finite element method (FEM), Ramaswamy and Jue [10] studied the thermocapillary and buoyancy convection in a rectangular cavity with aspect ratio of 0.5, 1.0 and 2.0. Mundrane and Zebib [11] found that two-dimensional thermocapillary convection is stationary, with no transition to unsteady motion, Kanouff and Grief [12] considered a fluid layer with surface tension varying with temperature quadratically. They found that the thermocapillary convection in a square cavity with a flat surface is oscillatory when the Marangoni number is above a critical value. The oscillation was due to the existence of a maximum surface tension so that the thermocapillary force around this location gave rise to opposing vortices.

Numerical simulations of double-diffusive convection in a differentially heated tank filled with a density-stratified fluid have so far been limited to two dimensions. Lee and Hyun [13] used finite difference results to simulate the experiment of Chen et al. [3]. More recently, Wright and Shyy [14] simulated the same problem with a constant heat flux boundary using a composite grid method. Hyun et al. [15] applied a Chebyshev collocation method to simulate double diffusion in low Prandtl number fluids. A square cavity with insulating top and bottom surfaces and isothermal (differential heating) sidewalls was considered. Results were obtained for Al–Cu and Pb–Sn alloys. Most recently, Chen and Liou [16] studied the problem of lateral heating of a stably stratified fluid in an inclined layer.

In the following, the experimental apparatus, procedure, and results are presented in Section 2. The equations, methods and results of the numerical simulations are presented in Section 3, followed by the conclusions in Section 4.

2. Experiments

2.1. Apparatus and procedure

Experiments were carried out in a shallow tank 5 cm wide × 1cm high × 10 cm long. The two sidewalls (10 × 1 cm) were made of chrome-plated copper, with passages provided for circulating fluid from two constant-temperature baths. The two endwalls and the bottom were made of Plexiglas. The fluid used was an ethanol–water solution; it was chosen because its free surface is not

easily contaminated. The concentration of the solution varied from 100 wt% ethanol at the top to 96 wt% at the bottom. This was achieved by injecting through a hypodermic needle three equal fluid layers with ethanol concentrations of 100, 98 and 96% successively. The needle was held perpendicularly with the exit just above the bottom boundary so that the lighter fluid was lifted upward by the inflow of heavier fluid. Each layer contained 16.7 cm^3 of fluid, and the injections were performed slowly to minimize mixing. The filled tank was not disturbed for 30 min so that diffusion could smooth out the sharp gradients between the layers. Since we have no means of measuring the concentration of ethanol, the diffusion process was simulated by a one-dimensional calculation, taking into account the effect of variable diffusivity. The concentration distribution 30 min after the start of the diffusion process was essentially linear with height, with non-diffusive effects near the top and bottom. With these results in mind, all experiments were begun 30 min after completion of the filling process. The thermophysical properties of a 98% ethanol–water solution were obtained from Landolt and Bornstein [17] and Weast [18] and are listed in Table 1.

Flow visualization was carried out by particle traces with aluminium powder as the tracer. The particles were mixed into the prepared solutions for each layer prior to filling of the tank. A 20-mW He–Ne laser with a cylindrical lens was used to provide a sheet of light through the tank. A CCD video camera was used to image the particle path, which was viewed on a monitor and simultaneously recorded by a VCR. Both vertical and horizontal views were observed. For the horizontal view, the CCD camera was mounted vertically above the tank. The test tank was mounted on a platform capable of vertical motion. In this manner, particle traces could be viewed at any horizontal plane within the 1-cm height of the test tank. For the vertical view, we used a mirror mounted at 45° to turn the light sheet to vertical and perpendicular to the hot and cold sidewalls. The mirror mount could be translated back and forth to obtain different vertical sections along the length of the tank. The CCD camera was mounted horizontally perpendicular to the laser sheet. A schematic diagram of the experimental setup is shown in Fig. 1.

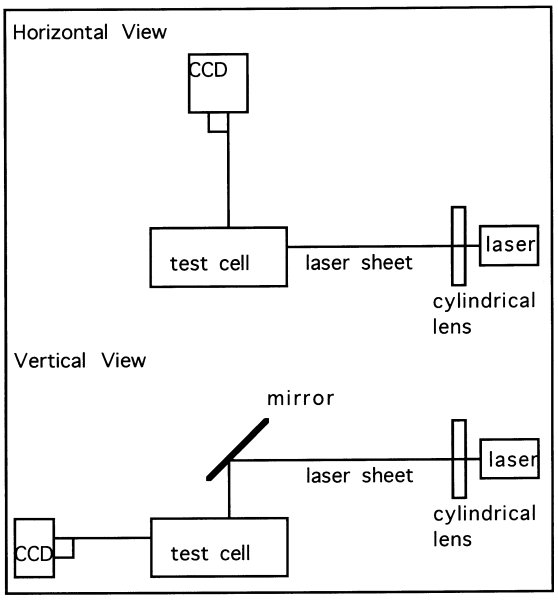

Fig. 1. Schematic diagram of the experimental setup.

2.2. Experimental results

The first set of experiments was conducted to determine the temperature difference needed to cause the onset of buoyancy-driven convection in the tank. In these experiments, a cover was placed at the top of the test tank to provide a rigid surface boundary condition. The temperature difference, ΔT, between the two sidewalls was increased 1°C every 40 min by adjusting the temperatures of the hot and cold walls simultaneously by $\pm\Delta T/2$. The time period of 40 min is the thermal diffusion time for a distance of 1.4 cm in ethanol, which is much larger than the size of the initial vortices near the cold and hot walls. Due to the stabilizing effect of the concentration stratification, no perceptible motion was observed throughout the tank until the ΔT reached 4°C.

For experiments with a free surface, capillary motion started along the surface when ΔT reached 2°C. This ΔT is higher than that ($\sim$ 1°C) needed to induce motion in

Table 1
Thermophysical properties of a 98% ethanol–water solution at 20°C

$\rho = 795.5$ [kg m^{-3}]	$\beta_T = 0.108 \times 10^{-2}$ [K^{-1}]
$\nu = 0.163 \times 10^{-5}$ [m^2 s^{-1}]	$Pr = \nu/\kappa = 19.1$
$\kappa = 0.854 \times 10^{-7}$ [m^2 s^{-1}]	$Le = \kappa/D = 77.2$
$D = 0.1106 \times 10^{-8}$ [m^2 s^{-1}]	[1]$\sigma_T = 0.88 \times 10^{-4}$ [N m^{-1} K^{-1}]
[2]$\beta_S = 0.38 \times 10^{-2}$ [wt%$^{-1}$]	[2]$\sigma_S = -0.117 \times 10^{-3}$ [N m^{-1} wt%$^{-1}$]

[1] For a 96% ethanol–water solution. Data from Weast [18].
[2] wt% of H_2O.

a deep tank [1], probably because of the proximity of the bottom wall. Soon after the surface motion started, finger convection in longitudinal rolls, similar to those seen in the deep tank, was observed. We recorded particle traces in the horizontal and the vertical planes at four different times in two separate experiments, S-20 and S-23, with the same initial stratification and $\Delta T = 2^{\circ}\mathrm{C}$. The experimental parameters for these two experiments are listed in Table 2.

The horizontal views of experiment S-23 are shown in the left column of Fig. 2. The laser light sheet was positioned 2 mm below the free surface. The camera was zoomed in to show approximately the middle 5-cm section of the tank. The cold (hot) wall appears on the right (left), and the motion is from left to right. All photos were taken at an 8-s exposure. The $2^{\circ}\mathrm{C}$ ΔT was imposed at 09:10 h. Two minutes later, at 09:12 h, finger convection was starting near the cold wall. At 09:14 h, these fingers became better organized. At 09:20 h, 10 min after the start of the experiment, finger convection was at its fully developed state, extending from the cold to the hot wall with vigorous mixing. (We note here that the adjustment of the cylindrical lens system was not perfect, thus the region near the hot wall was less illuminated.) Finger convection persisted to $\sim$ 09:35 h, and then it started to decay. By 09:50 h, 40 min after the start of the experiment, the fingers were gone.

The particle traces in the vertical plane of experiment S-20 are presented in the right column of Fig. 2. The vertical laser light sheet was positioned in the middle of the tank, and the cold wall appeared on the left. The exposure time for these four photos was 4 s, and they were taken approximately the same time into the experiment as those for experiment S-23. The experiment was started at 10:37 h. At 10:39 h, there was a large vortex near the cold wall, while there was hardly any motion near the hot wall. This is due to the fact that the surface tension increases with increasing concentration of water. Initially, the thermocapillary motion generated two small vortices, one each at the hot and cold wall. The one at the hot wall induced a flow upward along the hot wall and brought more water-concentrated fluid to the surface, thus reducing the surface tension gradient there. At the cold wall, however, the water-concentrated fluid brought up to the surface flows toward the cold wall, thus reinforcing the thermocapillary effect and increasing the surface tension gradient at the cold wall. These opposing effects are discussed further in the numerical simulation section. The finger-induced motion is indicated by the vertical velocity components of the particles in the mid-portion of the tank. At 10:42 h, 5 min into the experiment, the large convection cell deepened and reached the hot wall. More vertical motion was seen in the cell. The fluid in the lower portion of the tank remained stably stratified and motionless. At 10:46 h, the lower quiescent region diminished and there were a number of vortices in the convection cell. At 11:25 h, 38 min into the experiment, the flow pattern was similar to that in a homogeneous fluid layer, except for a small wedge of quiescent fluid near the hot wall. However, the inhomogeneity of the remaining concentration was reflected by the undulating particle lines near the free surface.

3. Numerical simulations

The simulations were carried out for the same cross-sectional geometry as for the experimental tank, with the same nondimensional parameters as in the experiments.

3.1. Equations and methods of solution

The two-dimensional fluid flow equations are cast in vorticity and stream function form. The dimensionless equations are

$$\frac{\partial \omega}{\partial t} + \frac{\partial}{\partial x}(u\omega) + \frac{\partial}{\partial y}(v\omega) = Pr(\nabla^2 \omega) + Pr\left(Ra_T \frac{\partial T}{\partial x} - Ra_S \frac{\partial S}{\partial x}\right) \quad (1)$$

$$\nabla^2 \psi = -\omega \quad (2)$$

$$\frac{\partial T}{\partial t} + \frac{\partial}{\partial x}(uT) + \frac{\partial}{\partial y}(vT) = \nabla^2 T \quad (3)$$

$$\frac{\partial S}{\partial t} + \frac{\partial}{\partial x}(uS) + \frac{\partial}{\partial y}(vS) = Le\nabla^2 S \quad (4)$$

with the dimensionless parameters

$$Pr = \frac{\nu}{\kappa}, \quad Le = \frac{\kappa}{D}, \quad (5)$$

$$Ra_T = \frac{g\beta_T H^3 \Delta T}{\nu\kappa}, \quad Ra_S = \frac{g\beta_S H^3 \Delta S}{\nu\kappa}.$$

To render the equations nondimensional, we used the

Table 2
Experimental conditions for S-20 and S-23

ΔT	ΔS	Ra_T	Ra_S	M_T	M_S
$2^{\circ}\mathrm{C}$	4%	152 000	845 000	15 900	−42 200

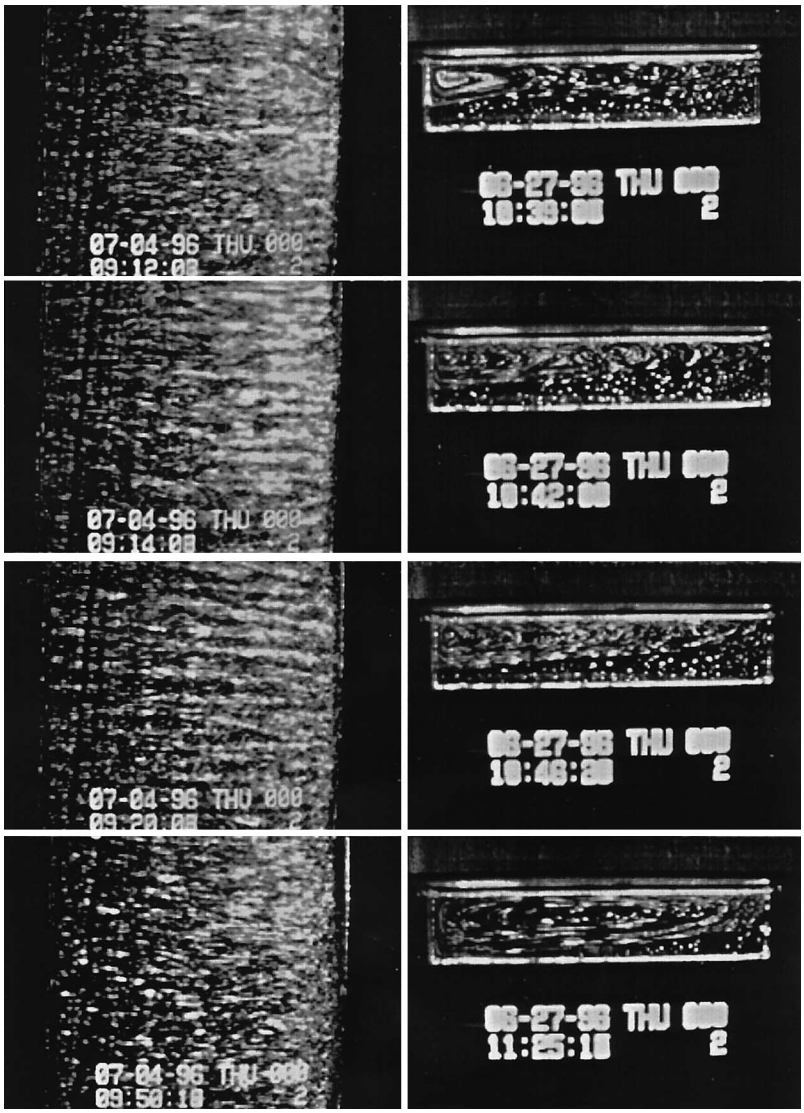

Fig. 2. Horizontal and vertical views of particle trace obtained in a stratified ethanol–water layer. Left column: horizontal view at 2 mm below the free surface, with the cold wall on the right, showing salt-finger convection. Photographs taken with an 8-s exposure. Right column: vertical view at the middle of the tank, with the cold wall on the left, showing the development of the convection cell originating at the cold wall. Photographs were taken with a 4-s exposure.

following characteristic quantities: the height H for length, H^2/κ for time, κ/H for velocity, ΔT for temperature, and ΔS for solute (water). With the cold wall at $x=0$, the hot wall at $x=5$, and the top and bottom boundaries at $y=1$ and 0, respectively,

$$x=0;\quad u=v=0,\quad T=0.5,\quad \frac{\partial S}{\partial x}=0 \tag{6}$$

$$x=5;\quad u=v=0,\quad T=-0.5,\quad \frac{\partial S}{\partial x}=0 \tag{7}$$

$$y=0;\quad u=v=0,\quad \frac{\partial T}{\partial y}=0,\quad \frac{\partial S}{\partial y}=0 \tag{8}$$

$$y=1;\quad \frac{\partial u}{\partial y}=-M_T\frac{\partial T}{\partial x}-M_S\frac{\partial S}{\partial x}=0,\quad \frac{\partial T}{\partial y}=0,\quad \frac{\partial S}{\partial y}=0 \tag{9}$$

in which the thermal and solutal Marangoni numbers are defined as

$$M_T=\frac{\sigma_T H\Delta T}{\mu\kappa},\quad M_S=\frac{\sigma_S H\Delta S}{\mu\kappa}$$

with the surface tension, γ, assumed to be linear functions of T and S,

$$\gamma=\gamma_0-\sigma_T(T-T_0)-\sigma_S(S-S_0). \tag{10}$$

The initial conditions are

$$t = 0; \quad u = v = 0, \quad S = 1 - y. \tag{11}$$

We note here that the linear distribution solute assumed in the simulation differs from the s-shaped distribution in the actual experiments. The finite difference method (FDM) [19] is used to solve these equations. The Laplacian operator is discretized using a central difference, the convection term is approximated by an upwind difference, and the time marching is modeled by the Crank–Nicholson method. The discretized equations are solved by successive over-relaxation (SOR), which is parallelized using a domain decomposition method. The algorithm is validated using previous results [20] for the square cavity problem. The vorticity predictions along the moving boundary are within 0.1%.

3.2. Simulation results

Three cases were calculated, and their dimensionless parameters are listed in Table 3. Case 1 corresponds to the actual experiments, Case 2 corresponds to the zero gravity condition, and Case 3 represents the absence of surface tension forces. A uniform grid with 81×401 nodes was used. The nondimensional time increment was 10^{-5}. Further refinement of the grid size was done, but with no significant changes. For all these cases, the calculations were carried out to $t = 0.10$, which corresponds to 117 s, approximately the time when finger convection was first observed.

We begin by looking at Case 1, the actual experiment. Figure 3 shows a sequence of gray-scale concentration contour maps as time evolves. Because of the low mass diffusivity, the concentration contours represent the fluid motion rather nicely. The growth of the vortex near the cold sidewall is evident. However, the vortex near the hot sidewall is contained near the upper corner and does not grow. In fact, on closer examination, the motion is oscillatory; this will be discussed later.

The growth of the vortex near the cold sidewall, as shown in Fig. 3, is very similar to the experimental observations in Fig. 2. The triangular shape of the vortex is due to the buoyancy effect of the stably stratified distribution. The heavy fluid at the bottom provides an upward thrust and pushes the vortex, forming a triangular shape.

Table 3
List of parameters for the simulation cases considered

Parameters	Case 1	Case 2	Case 3
Pr	17	17	17
Le	85	85	85
Ra_T	200 000	0	200 000
Ra_S	800 000	0	800 000
M_T	20 000	20 000	0
M_S	−40 000	−40 000	0

At the beginning, the imposed cooling and heating of the sidewalls induce very strong temperature gradients near the walls, as shown in Fig. 4a. As a result, two vortices form because of buoyancy and surface tension forces. These vortices bring high-concentration solution to the free surface, creating a nonuniform concentration on the free surface (Fig. 4b). Near the hot wall, the concentration on the free surface produces a surface tension force opposing the thermocapillary force. It is this competition that leads to oscillatory motion. On the other hand, the concentration on the free surface near the cold sidewall reinforces the thermocapillary force. This can be seen clearly in Fig. 4c, where the total surface tension effect $[(M_S/M_T)S - T]$ is plotted. The vortex near the cold sidewall therefore grows and further distorts the temperature and concentration fields.

The vertical temperature distribution near the cold wall ($x = 0.25$), Fig. 5a, is stabilizing. The vertical concentration distribution, Fig. 5b, is initially stably stratified. However, at later times, the rotation brings high-concentration solution to the top, creating a destabilizing effect. The total vertical density distribution $[(Ra_S/Ra_T)S - T]$ is plotted in Fig. 5c. The top-heavy situation can be seen clearly near $y = 0.9$. However, in the physical experiment, the positive solute concentration gradient, together with the stable temperature gradient, would have triggered the onset of finger convection, thus preventing the density inversion to occur. The salt fingers onset near the cold wall and gradually propagate throughout the tank, as observed in our experiments.

Let us now focus our attention on the hot sidewall. As pointed out earlier, the vortex is contained in the upper corner. The thermocapillary force due to the imposed temperature condition starts the rotation. The vortex transports high-concentration fluid to the free surface. The surface tension due to the nonuniform concentration distribution acts against the thermocapillary force. This competition gives rise to an oscillatory motion as shown in Fig. 6. Figure 6a shows the u-velocity profile vs y for different times near the hot sidewall (at $x = 4.75$). The surface ($y = 0$) u-velocity at the same x-location vs time is plotted in Fig. 6b. The oscillation is not exactly periodical. Also, oscillations subside after five cycles at approximately $t = 0.45$. A Fast Fourier Transform (FFT) of the data from $t = 0.0$ to $t = 0.0635$, as shown in Fig. 6c, reveals that the most dominant period is around 0.009 (~ 10.5 s), which is quite obvious from Fig. 6b. The other two peaks, with much lower amplitude, correspond to periods of 0.003 and 0.0018. The maximum at zero wave number is caused by the fact that the oscillation dies out very quickly.

Case 2 corresponds to a zero gravity condition, the motion is driven by the surface tension forces only, and there is no finger convection due to the absence of gravity.

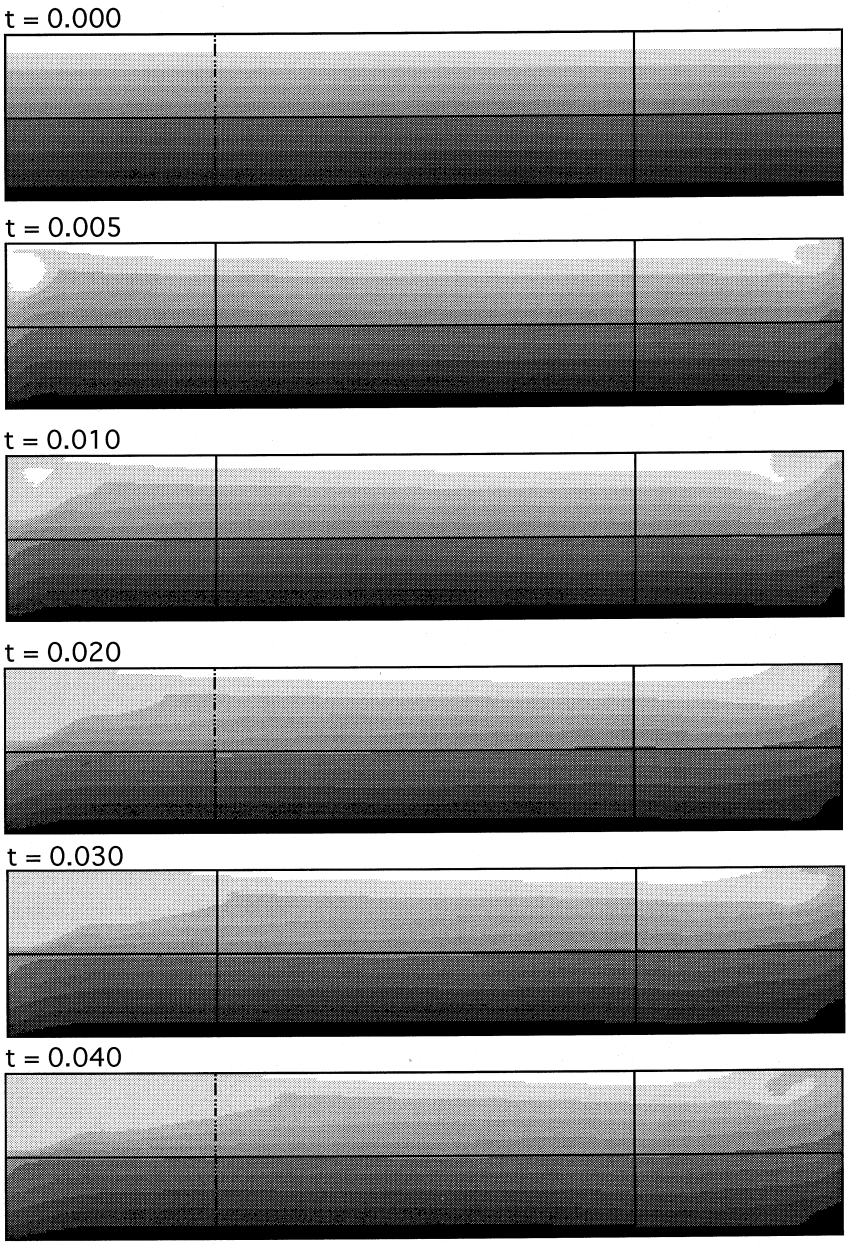

Fig. 3. Time evolution of concentration for Case 1.

The time sequence of the concentration contour is shown in Fig. 7. Similar to Case 1, the vortex near the cold sidewall grows and propagates toward the hot sidewall. The vortex near the hot sidewall, on the other hand, remains contained. The growing vortex from the cold wall, however, is no longer triangular because of the absence of a buoyancy effect. The oscillatory motion near the hot sidewall can be observed clearly from undulating concentration-level surfaces in Fig. 7. It can also be observed that the oscillating vortex is travelling downstream to the left. The u-velocity profile vs y for different times at $x = 4.75$ are plotted in Fig. 8a. The surface ($y = 0$) u-velocity at the same x-location vs time is plotted in Fig. 8b. The oscillation is much more complicated than that of Case 1. The FFT as shown in Fig. 8c reinforces this observation, as there are many more peaks. It is

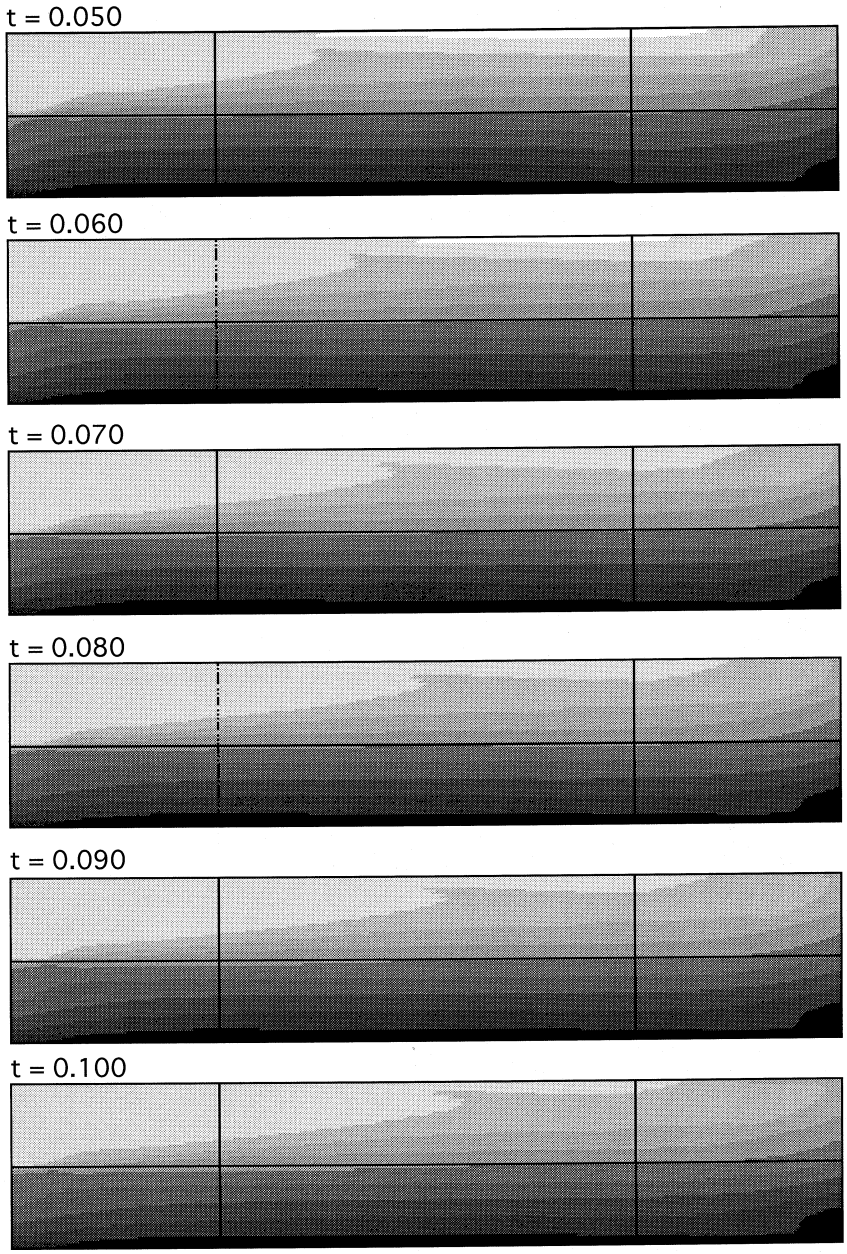

Fig. 3. *Continued.*

interesting that the highest peak corresponds to a period of 0. 009, which is identical to that of Case 1.

Case 3 corresponds to negligible surface tension effects. The motion is driven solely by the buoyancy forces. The time sequence of the concentration contour is shown in Fig. 9. There is essentially no motion in the tank except for the small vortices near the cold and hot sidewalls. The fact that the solutal Rayleigh number is four times larger than the thermal Rayleigh number means the stratification is very stable, thus the buoyancy-induced motion is nearly suppressed, except near the sidewalls. As a result, the vortices are growing relatively slower. In the absence of the surface forces, the oscillatory motion is no longer observed.

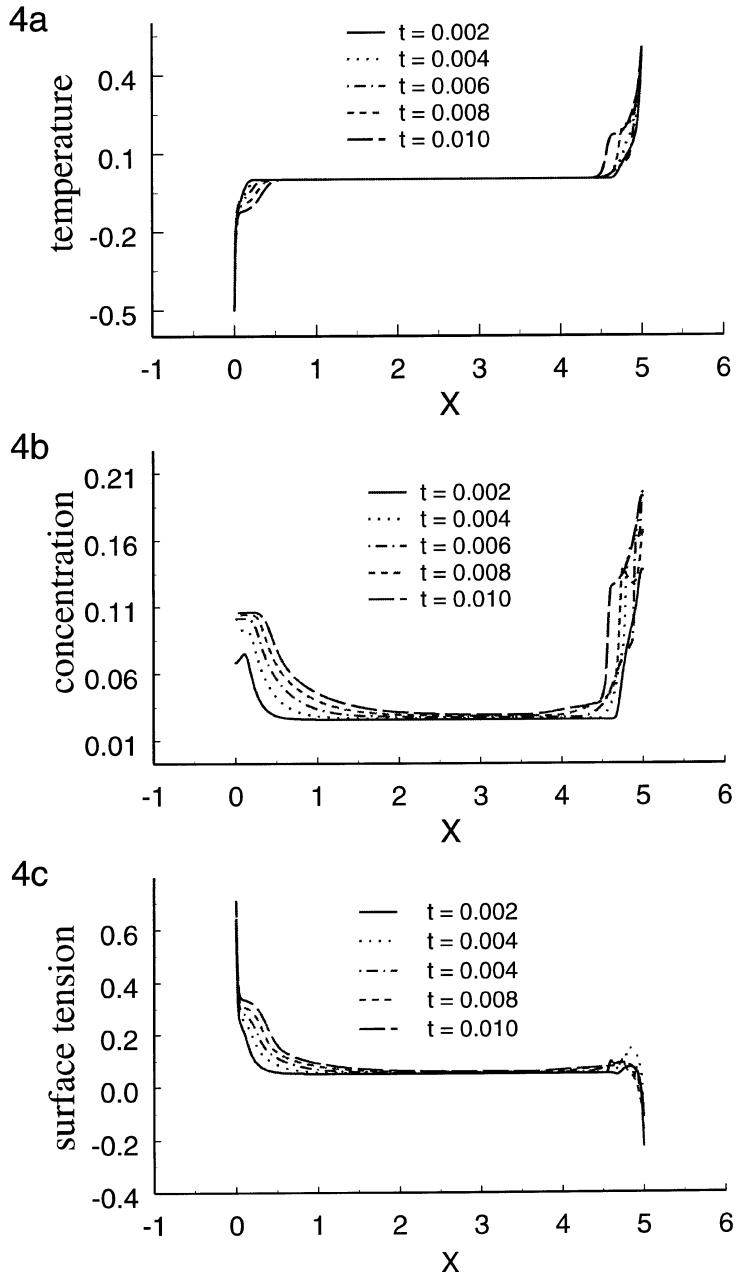

Fig. 4. Temperature, concentration and surface tension distributions on the free surface for Case 1.

4. Conclusions

From the results of our experimental and numerical investigations, the following conclusions can be drawn:

(1) Finger convection can be generated by capillary motion in a shallow layer of stratified fluid with a maintained small lateral temperature difference.

(2) In the ethanol–water solution used for the experiment, surface tension is increased by solute concentration. Because of this property, the thermal capillary motion is enhanced by the solutal capillary motion at the cold wall.

(3) As a result of (2), finger convection onsets at the cold wall and propagates toward the hot wall.

(4) Oscillatory motion is generated near the hot wall by

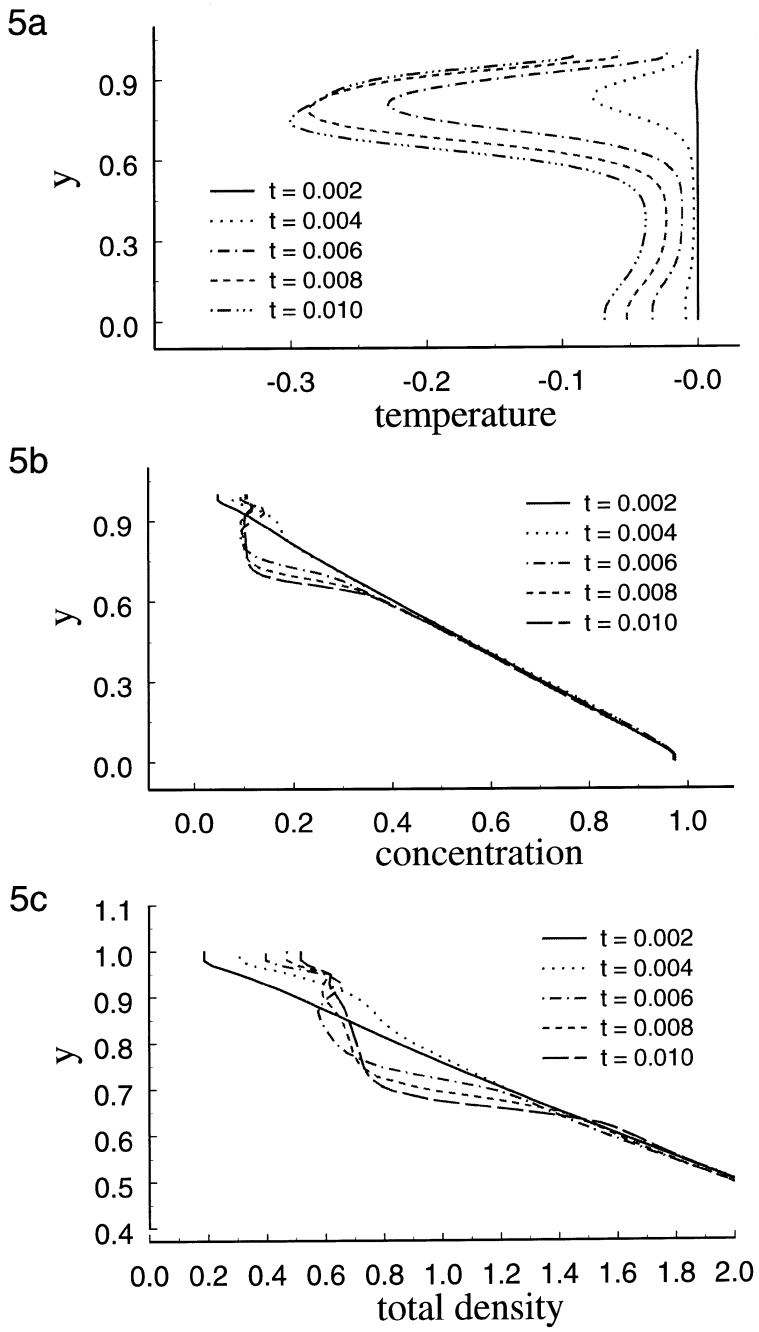

Fig. 5. Vertical distributions of temperature, concentration and total density near the cold wall at $x = 0.25$ for Case 1.

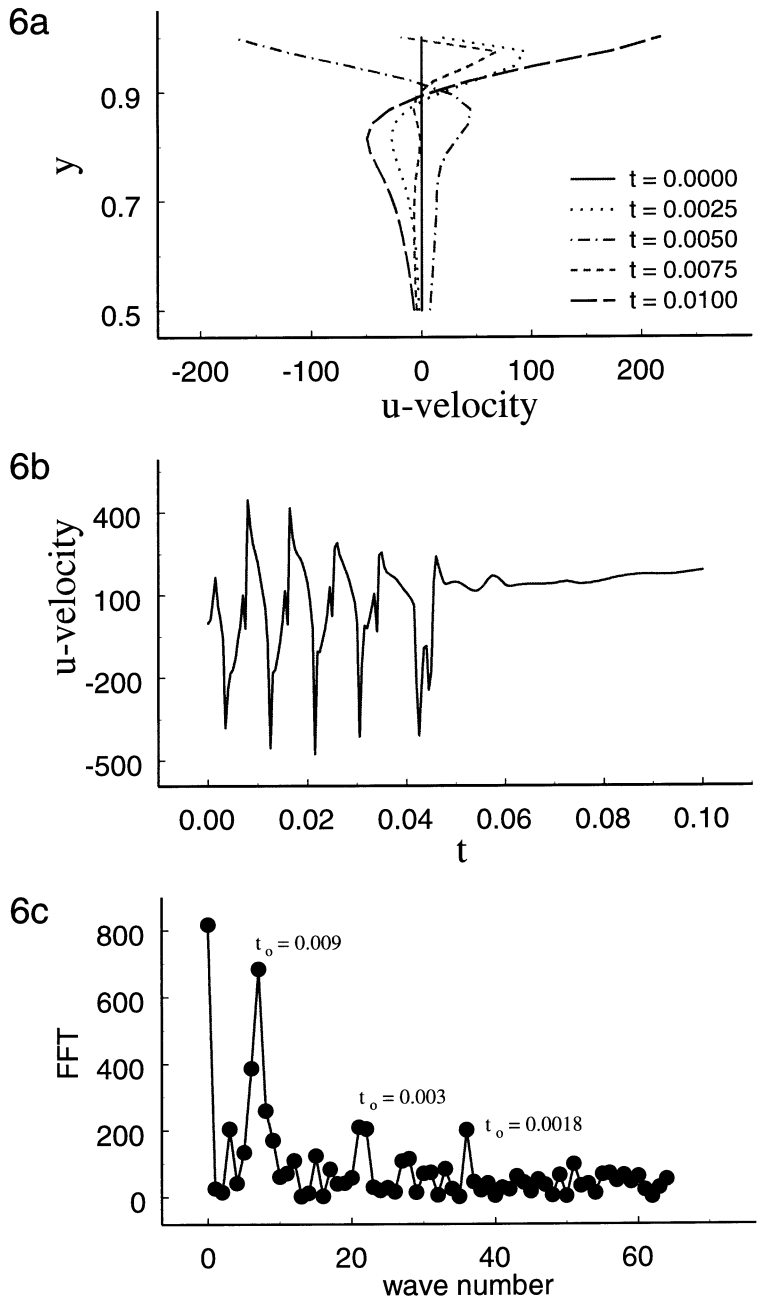

Fig. 6. Case 1: (a) *u*-velocity vs *y* at $x = 4.75$; (b) surface *u*-velocity vs *t* at $x = 4.75$; (c) FFT spectrum for (b).

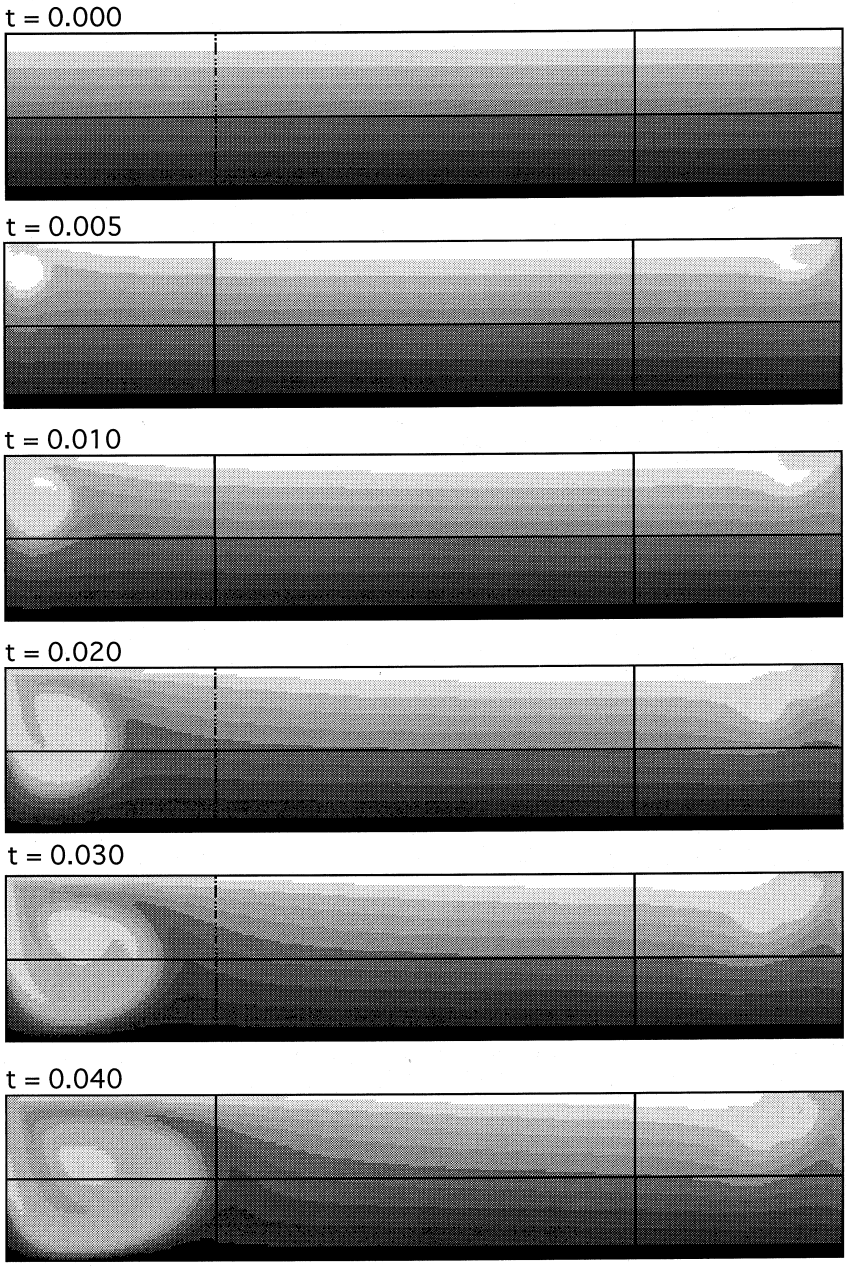

Fig. 7. Time evolution of concentration contours for Case 2.

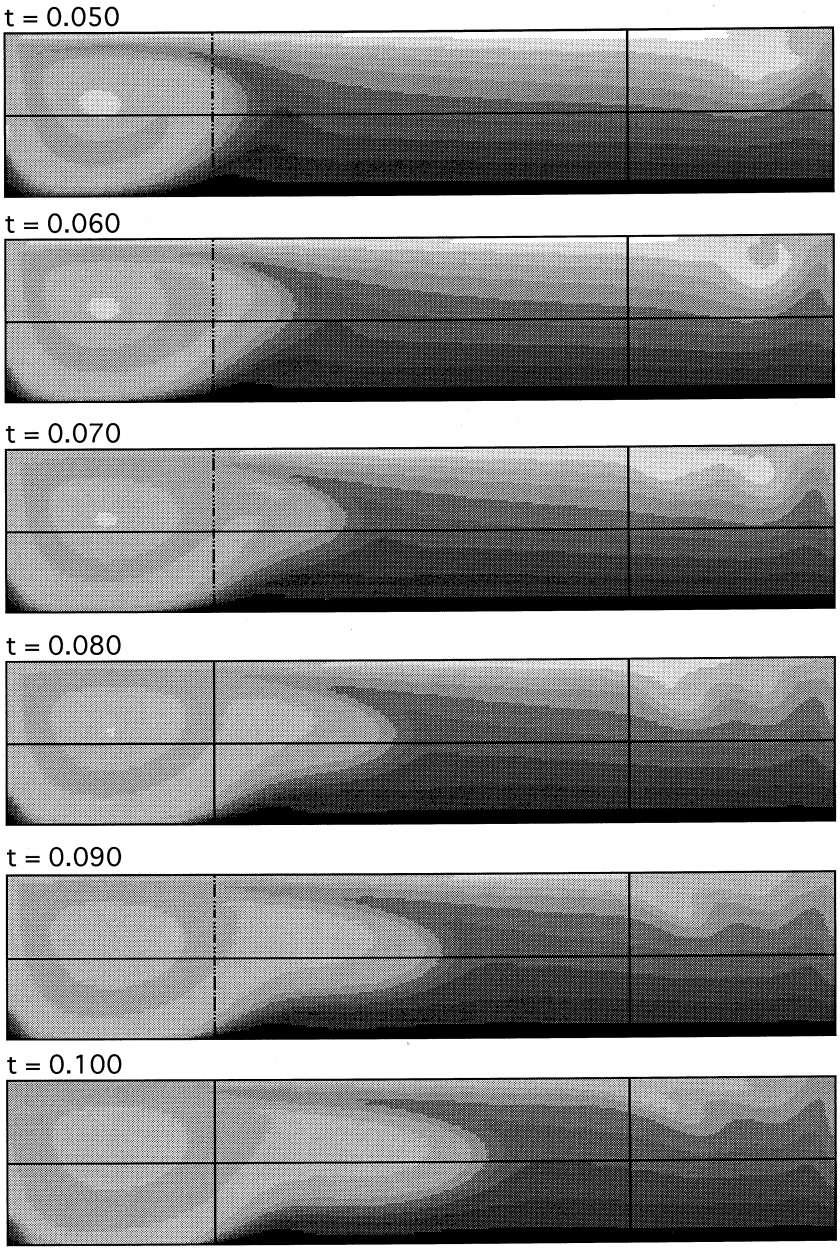

Fig. 7. *Continued.*

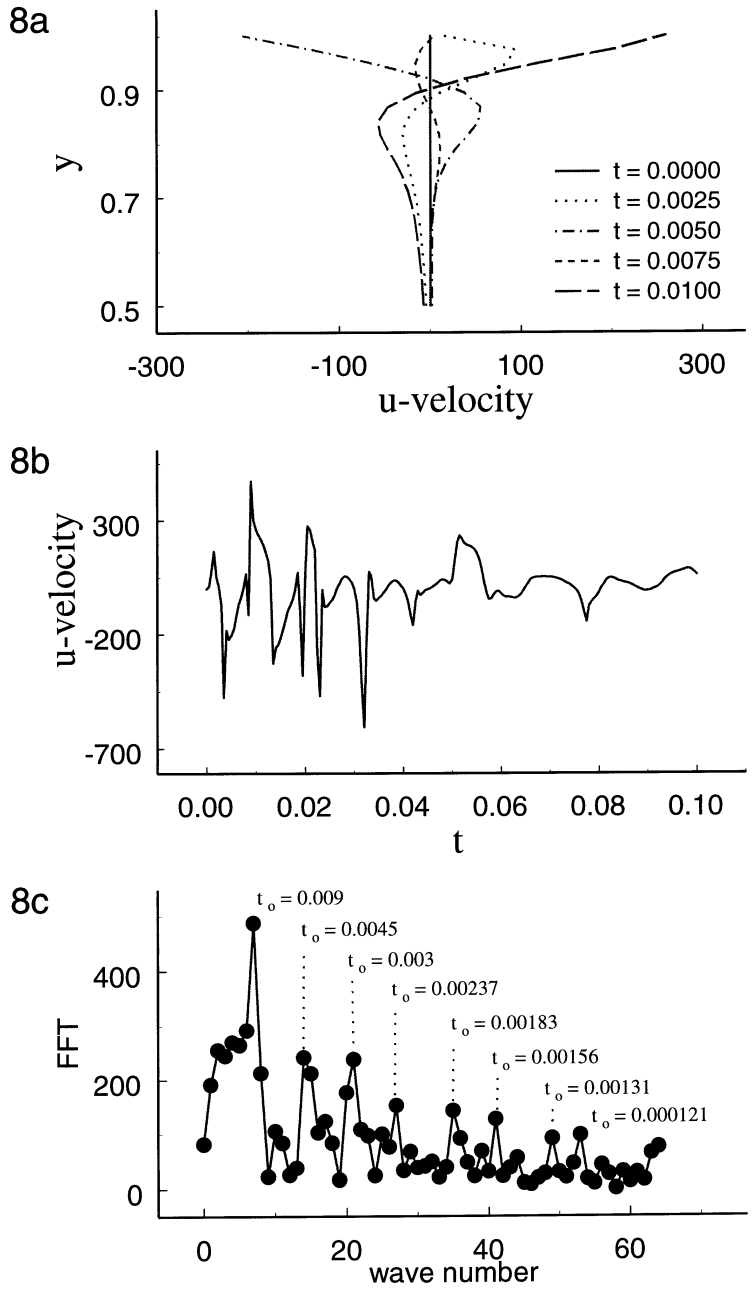

Fig. 8. Case 2: (a) u-velocity vs y at $x = 4.75$; (b) surface u-velocity vs t at $x = 4.75$; (c) FFT spectrum for (b).

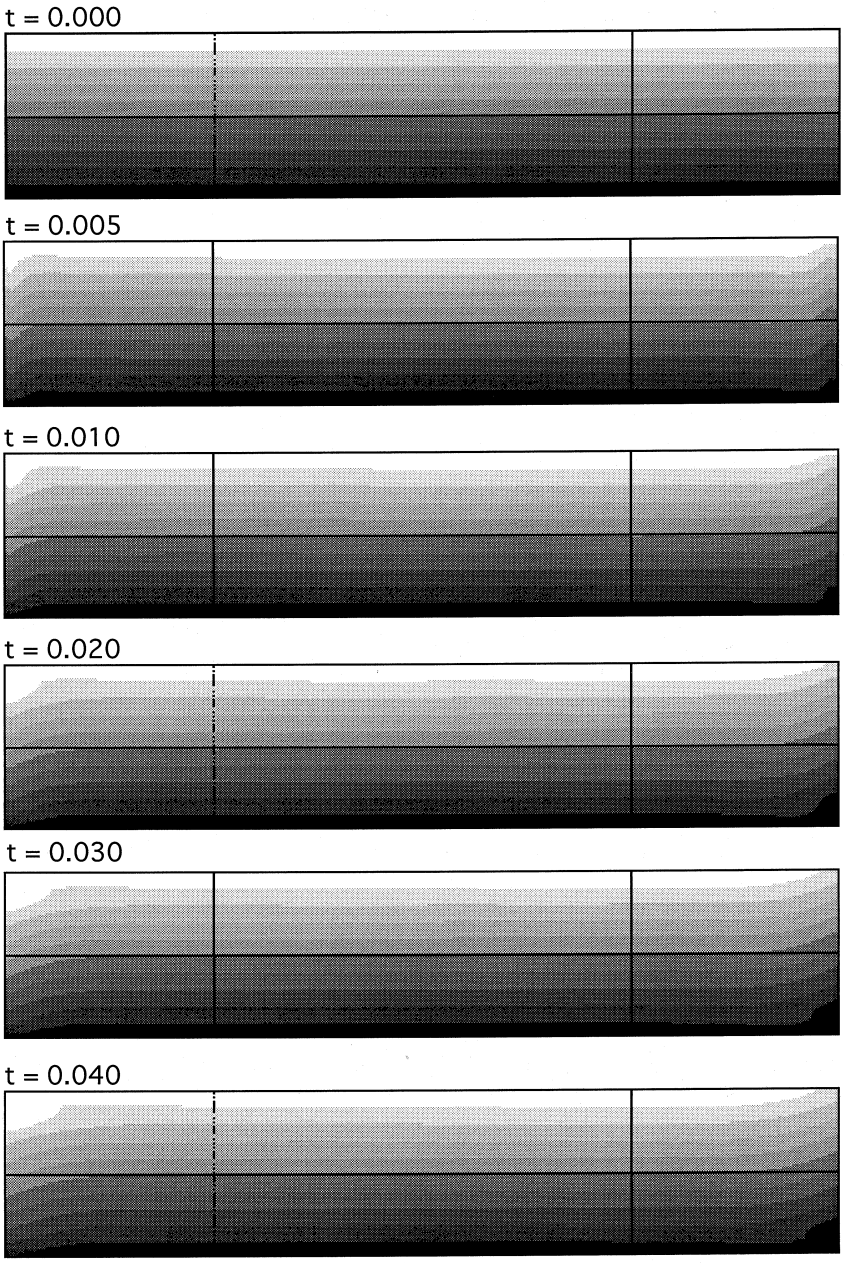

Fig. 9. Time evolution of concentration contours for Case 3.

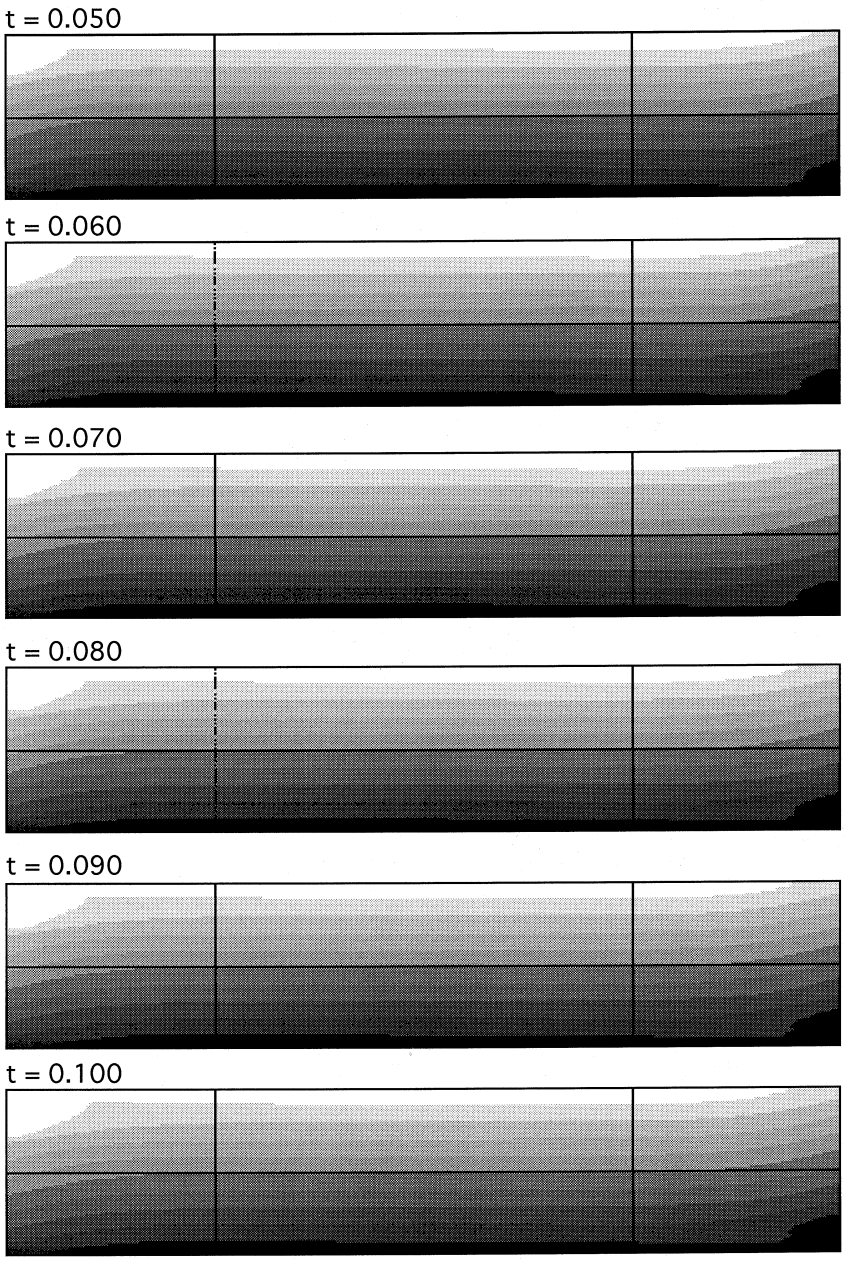

Fig. 9. *Continued.*

the opposite effects of thermal and solutal capillarity. The dominant oscillation period was found by FFT to be 10.5 s.

(5) Information provided by a two-dimensional simulation during the early stages of convection greatly aids our understanding of the observed flow phenomenon.

Acknowledgements

This research was funded by NASA through Microgravity Science and Application Grant NAG-1328. The computations were performed at the Maui High Performance Computing Center.

References

[1] C.F. Chen, F. Chen, Salt finger convection generated by lateral heating of a solute gradient, Journal of Fluid Mechanics 352 (1997) 161–176.

[2] S.A. Thorpe, P.K. Hutt, R. Soulsby, The effects of horizontal gradients on thermohaline convection, Journal of Fluid Mechanics 38 (1969) 375–400.

[3] C.F. Chen, D.G. Briggs, R.A. Wirtz, Stability of thermal convection in a salinity gradient due to lateral heating, International Journal of Heat and Mass Transfer 14 (1971) 57–65.

[4] P.F. Linden, Salt fingers in steady shear flow, Geophys. Fluid Dyn. 6 (1974) 1–27.

[5] S. Thangam, C.F. Chen, Salt-finger convection in the surface discharge of a heated saline jet, Geophys. Astrophys. Fluid Dyn. 18 (1981) 111–146.

[6] S.A. Piacsek, J. Toomre, Nonlinear evolution and structure of salt fingers, in: J.C.J. Nihoul (Ed.), Marine Turbulence, Elsevier, New York, 1980, pp. 193–219.

[7] C.Y. Shen, The evolution of the double-diffusive instability: salt fingers, Physics of Fluids A 1 (1989) 829–844.

[8] C.Y. Shen, G. Veronis, Scale transition of double-diffusive finger cells, Physics of Fluids A 3 (1991) 58–68.

[9] H.B. Hadid, B. Roux, Thermocapillary convection in long horizontal layers of low-Prandtl-number melts subject to a horizontal temperature gradient, Journal of Fluid Mechanics 224 (1990) 77–103.

[10] B. Ramaswamy, T.C. Jue, Analysis of thermocapillary and buoyancy-affected cavity flow using FEM, Numerical Heat Transfer, Part A 22 (1992) 379–399.

[11] M.R. Mundrane, A. Zebib, Oscillatory buoyant thermocapillary flows, Physics of Fluids A 6 (1994) 3294–3305.

[12] M. Kanouff, R. Greif, Oscillations in thermocapillary convection in a square cavity, International Journal of Heat and Mass Transfer 37 (1994) 885–892.

[13] J.W. Lee, J.M. Hyun, Time-dependent double diffusion in a stably stratified fluid under lateral heating, International Journal of Heat and Mass Transfer 34 (1991) 2409–2421.

[14] J. Wright, W. Shyy, Numerical simulation of unsteady convective intrusions in a thermohaline stratification, International Journal of Heat and Mass Transfer 39 (1996) 1183–1201.

[15] M.T. Hyun, D.C. Kuo, T.L. Bergman, K.S. Ball, Direct simulation of double diffusion in low Prandtl number liquids, Numerical Heat Transfer Part A 27 (1995) 639–650.

[16] Y.-M. Chen, J.-K. Liou, Time-dependent double-diffusive convection due to salt-stratified fluid layer with differential heating in an inclined cavity, International Journal of Heat and Mass Transfer 40 (1997) 711–725.

[17] H. Landolt, R. Bornstein, Eigenschaften der Materie in ihren Aggregatzustanden, 5 Teil, Springer-Verlag, 1989.

[18] R.C. Weast, (Ed.), Handbook of Chemistry and Physics, CRC Press, Boca Raton, 1975.

[19] D.A. Anderson, J.C. Tannehill, R.H. Pletcher, Computational Fluid Mechanics and Heat Transfer, Hemisphere, New York, 1984.

[20] U. Ghia, K.N. Ghia, C.T. Shin, High-Re solutions for incompressible flow using the Navier–Stokes equations and a multigrid method, Journal of Computational Physics 48 (1982) 387–411.